Chemical Engineering Journal 458 (2023) 141471

Contents lists available at ScienceDirect

Chemical Engineering Journal

journal homepage: www.elsevier.com/locate/cej

# Silkworm cocoon waste-derived nitrogen-doped hierarchical porous carbon as robust electrode materials for efficient capacitive desalination

Su-Mei Zheng [a,b,c], Zhi-Hua Yuan [a,b], Dionysios D. Dionysiou [d], Lu-Bin Zhong [a,b], Fei Zhao [e], Jia-Cheng E. Yang [a,b,*], Yu-Ming Zheng [a,b,*]

[a] CAS Key Laboratory of Urban Pollutant Conversion, Institute of Urban Environment, Chinese Academy of Sciences, Xiamen, Fujian 361021, China
[b] University of Chinese Academy of Sciences, Beijing 100049, China
[c] The Higher Educational Key Laboratory for Flexible Manufacturing Equipment Integration of Fujian Province, Xiamen Institute of Technology, Xiamen, Fujian 361000, China
[d] Environmental Engineering and Science Program, Department of Chemical and Environmental Engineering (ChEE), University of Cincinnati, Cincinnati, OH 45221-0012, USA
[e] College of Environmental Science and Engineering, Nankai University, Tianjin 300350, China

ARTICLE INFO

*Keywords:*
Silkworm cocoon waste
Desalination
Capacitive deionization
Cocoon wastewater
Resource recovery

ABSTRACT

Capacitive deionization (CDI) has potential in desalination applications. However, developing a cost-effective and environmental-friendly CDI electrode is still challenging. Here, we report the synthesis of a tailored nitrogen-doped hierarchical porous carbon (NPC) derived from the waste silkworm cocoon and its promising use as a CDI electrode for desalination applications. Results show that both the graphitic N contents and defects (from $I_D/I_G$ values) within NPC-x regulated the intrinsic resistance and conductivity of NPC-x electrodes, thus giving graphitic N contents and defects-dependent CDI desalination performance. The optimized NPC-1.5 electrode exhibited an electrosorption capacity of 22.19 mg $g^{-1}$ with an average desalination rate of 1.1 mg $g^{-1}$ $min^{-1}$ (100 mg $L^{-1}$ of NaCl solution, an applied voltage of 1.2 V, and a flow rate of 40 mL $min^{-1}$). Such desalination performance is superior to the commonly reported activated carbon and other porous carbon electrodes under similar desalination conditions. Moreover, the optimized electrode can still maintain 97 % of its initial electrosorption capacity even after 50 cycles, indicating its outstanding reusability in the desalination application. This work shows a promising CDI electrode material of silkworm cocoon waste-derived porous carbon with highly efficient desalination performance, which will spark more efforts in the development of resource utilization-oriented desalination technologies.

## 1. Introduction

Capacitive deionization (CDI) has captured more and more attention in the field of wastewater desalination and selective ion removal by virtue of its high operability, energy/cost effectiveness, and environmental friendliness [1–7]. Unlike the traditional thermal-driven (or pressure-/electric-driven) desalination techniques, the desalination efficiencies of CDI devices are highly relying on the intrinsic structures and properties of the electrode materials [8]. Therefore, a wide variety of metal oxides, metal sulfides/carbides, redox-active polymer compounds, carbonaceous materials or their combined forms have been widely investigated to develop high-efficiency CDI electrodes [9–12]. Recently, using carbonaceous materials as the CDI electrodes has emerged as a prevailing research topic due to their high earth abundance and environmental compatibility [13,14]. However, there exist big challenges for rationally tailoring the carbon-based electrode materials with switchable hydrophilicity and hydrophobicity, high specific surface area, desirable pore size distribution, high conductivity, and/or robust electro-chemical stability.

It was found that heteroatomic doping engineering has the potential to improve the hydrophilicity and electrical conductivity of carbonaceous electrode materials, while to tune their pore/structure characteristics and chemical stability [15–23]. In recent years, there has been a research trend of using nitrogen-containing polymers and metal–organic

* Corresponding authors at: CAS Key Laboratory of Urban Pollutant Conversion, Institute of Urban Environment, Chinese Academy of Sciences, Xiamen, Fujian 361021, China.
*E-mail addresses:* jcyang@iue.ac.cn (J.-C.E. Yang), ymzheng@iue.ac.cn (Y.-M. Zheng).

https://doi.org/10.1016/j.cej.2023.141471
Received 25 September 2022; Received in revised form 4 January 2023; Accepted 13 January 2023
Available online 16 January 2023

frameworks to synthesize various *N*-doped carbon composite electrodes with improved CDI desalination performance [21–23]. For example, Cen et al. reported *N*-doped layered porous carbon (CHPC) with desirable macropores and mesopores via a mixed carbonization process of chitosan, colloidal $SiO_2$ and polytetrafluoroethylene [21]. The CDI desalination capacity of resultant CHPC was found to be 26.5 ± 1.5 mg $g^{-1}$, and the average desalination rate reached 8.8 ± 0.5 mg $g^{-1}$ $min^{-1}$. Meanwhile, zeolitic imidazolate frameworks (such as ZIF-8 and ZIF-67) can serve as nitrogen-containing precursors and structure-directing agents simultaneously to form porous *N*-doped carbon electrode materials to enhance the desalination capacity [22,23]. The combination of polymer and ZIF-8 can result in 3D interconnected heteroatom *N*-doped carbon tubes, thus giving an ultrahigh salt adsorption capacity and good reusability [22]. However, the aforementioned routes for the heteroatomic doping engineering are generally chemically and/or energy intensive, which undoubtedly become a bottleneck for the development of sustainable CDI desalination technologies. Therefore, it is highly desirable to develop a green and cost-effective method to prepare heteroatom-doped carbon electrode materials with tailored morphologies or pore structures.

Recently, more and more attention has been paid to the use of nitrogen-rich biomaterials/biomass as the precursors to synthesize heteroatomic doping electrode materials due to their environmental compatibility and the diversity of their functional groups [24–26]. For instance, the mushroom mycelia had been used as the starting material to fabricate a hierarchically porous nitrogen-doped carbon electrode with a superior desalination capacity of 24.17 mg $g^{-1}$ [25]. Interestingly, the nitrogen-rich eggshell membranes can be carbonized as a desalination electrode material to preferably adsorb $NO_3^-$ ions from water with a high selectivity of $NO_3^-/Cl^-$ (7.79) [26]. Meanwhile, natural silk has also been regarded as an attractive precursor to prepare hierarchically porous *N*-doped carbon (HPNC) electrode due to its abundant silk fibroin and lamella-like multiple layer structure [27]. However, the natural silk is expensive. Instead, silkworm cocoon waste (SCW) in the cocoon wastewaters can be a potential alternative to fabricate renewable and eco-friendly HPNC electrode. This is due to two facts: I) The nitrogen- and carbon-rich cocoon wastewaters with high protein content of up to 6,000 mg $L^{-1}$ were proven to be an appropriate precursor substance to form carbonaceous materials [28]. II) The SCW reclamation and reuse can directly reduce the discharge of cocoon wastewaters into the receiving water bodies [29,30]. Nevertheless, to the best of our knowledge, there is little information about using SCW-derived HNPC as a CDI electrode for desalination application, not to mention the structure and property-regulated desalination performance and mechanism.

Herein, using the silkworm cocoon waste (rich in the cocoon wastewater) as a source of nitrogen and carbon, we developed NPC-x via a $ZnCl_2$ activation-carbonization process, and unprecedentedly used them as electrode material for CDI desalination applications. The contents of graphitic N and defects within the folded and hierarchical NPC-x can be simply tuned by the concentrations of $ZnCl_2$, thus resulting in graphitic N and defect-dependent electronic resistance and CDI desalination capacity. Surprisingly, the optimized NPC-1.5 demonstrated superior desalination performance with an adsorption capacity of 21.9 mg $g^{-1}$ and an average adsorption rate of 1.1 mg $g^{-1}$ $min^{-1}$ (under a low NaCl solution of 100 mg $L^{-1}$ at an applied voltage of 1.2 V), surpassing most reported carbon-based electrodes under similar operating conditions. This work will stimulate more interest in fabricating various nitrogen-doped carbon electrode materials for desalination applications using cost-effective and environmentally friendly methods with less carbon footprint. Moreover, it will open new directions for the development of SCW utilization-oriented CDI desalination technologies.

## 2. Experimental

### 2.1. Materials and chemicals

Cocoon wastewater (CW) containing SCW was obtained from a silk reeling factory in Yizhou, Guangxi, China. The wastewater appeared tawny and turbid, and the solution pH was in the range 10–12. The $COD_{Cr}$ of CW was determined as 100,000–120,000 mg $L^{-1}$ with its protein content being 45,000–47,000 mg $L^{-1}$. *N*-methyl-2-pyrrolidone (NMP, >99 %), sodium fluoride (NaF, 99 %) and sodium chloride (NaCl, 99.5 %) were purchased from Shanghai Lingfeng Chemical Co., Ltd. Zinc chloride ($ZnCl_2$, 98 %), hydrochloric acid (HCl, 36–38 %), and other chemicals were provided by Sinopharm Chemical Reagents Co., Ltd. Carbon black and polyvinylidene fluoride (PVDF) were purchased from Jinqiushi Chemical Co. Ltd. All the chemicals, unless otherwise noted, were used without further purification. An anion exchange membrane (AEM) and a cation exchange membrane (CEM) were purchased from Xiamen Cleanwater Technology Co., Ltd. Deionized (DI) water (18.2 MΩ/cm) was used to prepare all the solutions for the fabrication of various electrode materials.

### 2.2. Fabrication of NPC-x

The CW mainly consists of SCW, and most SCW exists in its dissolved forms in CW. Firstly, 100 mL of CW was pumped and filtered to remove the suspended solids. Then, the corresponding mass of $ZnCl_2$ was added into CW filtrate to form a $ZnCl_2$-containing solution with different concentrations of 0.5 M, 1 M, 1.5 M and 2 M. Next, the resultant solution was put into a tubular furnace at 300 ℃ for 2 h to remove the moisture and tar. The solid precursor was heated at 900 ℃ for 1 h under a $N_2$ atmosphere (with the ramp rate of 5 ℃/min). The resultant black solid was ground into powder, which was subsequently immersed into a 0.5 M HCl solution to remove the zinc species. The obtained powder was then washed with plenty of deionized water until the filtered solution was neutral. The black product was dried at 120 ℃ for 12 h, and the final product was marked as NPC-x (x: 0.5 M, 1 M, 1.5 M and 2 M). For comparison, identical steps were repeated to obtain pure cocoon-derived nitrogen-doped hierarchical porous carbon (CNPC) (replacing CW with 6 g of pure cocoons as the precursors).

$ZnCl_2$ has a melting point of 732 ℃ and while the treatment temperature reaches up to 900 ℃, $Zn^{2+}$ will react with carbon to form $ZnCO_3$. $Zn^{2+}$ can erode the surface of carbon material and form a porous structure. The subsequent pyrolysis produces ZnO, $CO_2$ and CO. The release of $CO_2$ and CO further expands the pores and eventually forms porous microscopic morphology. The nanopores can provide large specific surface area and allow the formation of a large number of double layer adsorption active sites. All these are beneficial to deliver high double layer capacitance and speed up the adsorption rate. The transition metal $Zn^{2+}$ in $ZnCl_2$ has an empty d orbital, which could accept the lone pair electrons of N species in the protein molecules to form stable intermediates. Furthermore, in the pre-oxidation stage, protein and $Zn^{2+}$ intermediates can complete aromatization at a lower temperature and a shorter time. Thus, the stability of *N*-doped carbon materials can be enhanced in the pre-oxidation and carbonization process (Fig. 1a).

### 2.3. Materials characterization

The crystal structures of the samples were characterized by X-ray diffraction (XRD, D/max-2500) with the 2-theta diffraction angle ranging from 10° to 80°. The specific surface area and pore size distribution of NPC-x and CNPC were analyzed using a Brunauer-Emmett-Teller (BET) analyzer (BELSORP-max, Microtrac BEL Corp, Japan) under the condition of liquid nitrogen (77 K). The morphology structures of the samples were obtained by a scanning electron microscope (FESEM, S-4800, Hitachi, Japan). Raman spectroscopy (LabRAM Aramis, Horiba Jobin Yvon S.A.S., France) was used to examine the degree

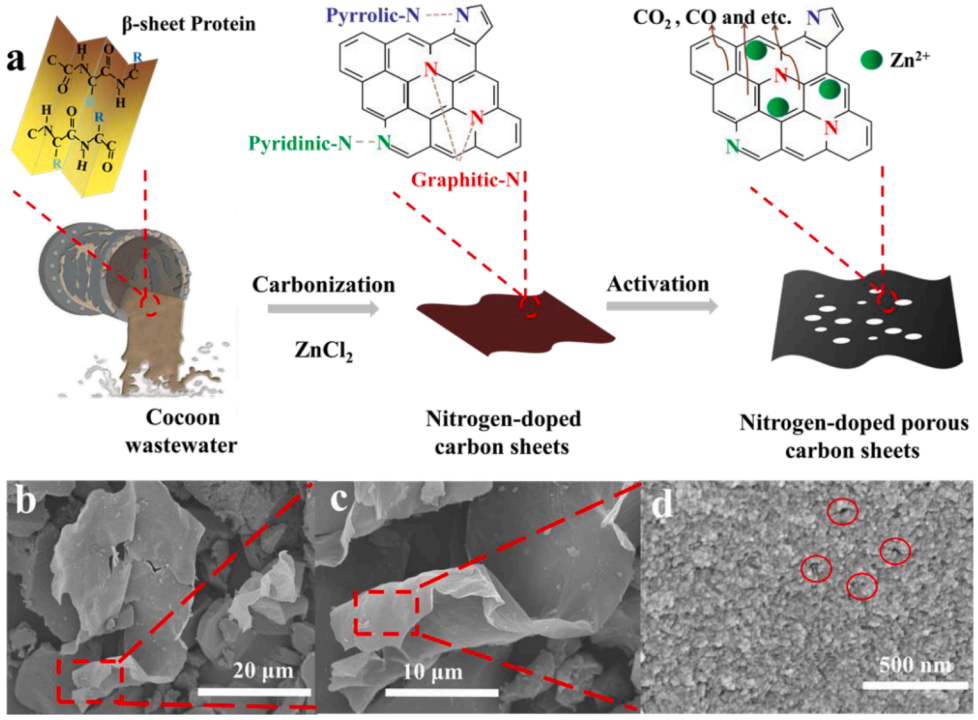


**Fig. 1.** (a) Schematic illustration of the preparation of NPC-x, (b-d) surface structures and morphologies of the optimized NPC-x.

of graphitization of NPC-x and CNPC. X-ray photoelectron spectroscopy (XPS, Shimadzu Corporation Axis Supra, Japan) was employed to probe the elemental composition within NPC-x and CNPC. The contact angles of NPC-x related CDI electrodes were measured by a goniometer (DSA30, KRUSS, German). The residual Zn in NPC-x and CNPC was measured by an Inductively Coupled Plasma Optical Emission Spectrometer (ICP-OES, Agilent 720).

### 2.4. Electrochemical characterization

The electrochemical measurements of samples were performed in the NaCl solution (1.0 mol/L) using an electrochemical station (CHI 660E, CH Instrument, Inc., Shanghai, China) at room temperature. The three-electrode configuration consisted of a Ag/AgCl reference electrode, a working electrode, and a Pt counter electrode. For the preparation of working electrode, NPC-x (80 wt%), poly(vinylidene fluoride) (PVDF, 10 wt%), and carbon black powder (10 wt%) were firstly dispersed in the solvent of *N*-methyl-2-pyrrolidone (NMP) using a magnetic mixer to form a paste-like slurry (after stirring for 2 h). Then, the slurry was coated onto a hydrophilic carbon paper (1 cm × 1 cm, mass loading: 1.0 mg $cm^{-2}$) by drop-casting. Lastly, the hybrid carbon paper was vacuum-dried at 80 °C for 12 h to obtain the working electrode. The tests of cyclic voltammetry (CV) and galvanostatic charge–discharge (GCD) were carried out with the potential range from 0 to 0.5 V at different scanning rates. Electrochemical impedance spectroscopy (EIS) measurements were conducted with the frequency ranged from 100 kHz to 0.01 Hz and an amplitude of 5.0 mV.

The specific capacitance ($C_{sp1}$, F/g) was calculated from the CV curves with the following equation:

$$C_{sp1} = \int \frac{IdV}{2v\Delta Vm} \tag{1}$$

where IdV is the integrated area of CV curve, while ΔV (V) is the scanning potential window. m (g) is the mass of activate material (like NPC and CNPC) within the working electrode, and v (V $s^{-1}$) is the scanning rate.

The specific capacitance ($C_{sp2}$, F/g) was calculated from the GCD curves with the following equation:

$$C_{sp2} = \frac{I \times \Delta t}{\Delta V \times m} \tag{2}$$

where I (A) is the current, and Δt (s) is the discharge time. ΔV (V) is the potential window, and m (g) is the mass of activate material (like NPC and CNPC) within the working electrode.

The $Na^+$ diffusion coefficient ($D_{Na+}$, $cm^2$ $s^{-1}$) was calculated by the following equation:

$$D_{Na^+} = \frac{R^2T^2}{2F^4c^2A^2\sigma^2} \tag{3}$$

$$Z_{re} = \sigma\omega^{-0.5} \tag{4}$$

where R is the ideal gas constant (8.314 J $K^{-1}$ $mol^{-1}$), T is the absolute temperature (K), F is the Faraday constant (96,485 C $mol^{-1}$), and c is the mass density of $Na^+$ within the electrode (mol $cm^{-3}$). A is the surface area of the working electrode ($cm^2$) and σ is the Warburg factor (Ω $s^{-0.5}$). $Z_{re}$ is the real part impedance (Ω) and ω is the frequency ($s^{-1}$).

### 2.5. Desalination experiments

The slurry for CDI electrode was prepared based on the above method for electrochemical characterization. Then, the as-prepared slurry was cast onto a pair of high purity titanium plates (coating area: 4 cm × 5 cm) and vacuum-dried at 80 °C for 12 h. The mass of the NPC-x within each electrode was approximately 40 mg. Lastly, the resultant electrodes were directly used for the batch-mode desalination experiments with 50 mL of 100–500 mg $L^{-1}$ NaCl solutions. A peristaltic pump was utilized to maintain the solution in a state of flow with a rate of 40 mL $min^{-1}$. The real-time concentration of NaCl was monitored by a conductivity meter (DDSJ-308F) at the outlet of the CDI cell. The concentration of NaCl can be obtained from the corresponding NaCl conductivity through mathematical calculations [31]. All the desalination experiments were operated in constant voltage mode and the voltage was set to 1.2 V. In order to further improve the SAC of NPC-1.5, a pair of

cation exchange membranes were added to design membrane capacitive deionization (MCDI) experiment.

The salt adsorption capacity (SAC, mg $g^{-1}$), average salt adsorption rate (ASAR, mg $g^{-1}$ $min^{-1}$), and charge efficiency (CE) were calculated by the following equations:

$$SAC = \frac{(C_0 - C_t)V}{m} \tag{5}$$

$$ASAR = \frac{SAC}{t} \tag{6}$$

where $C_0$ (mg $L^{-1}$) and $C_t$ (mg $L^{-1}$) are the concentrations of NaCl at the operation time of 0 and t min, respectively, while V (L) represents the total volume of NaCl solution. m (g) is the mass of the active material in the two electrodes, and t (min) is the operation time.

$$CE = \frac{SAC \times m \times F}{\int Idt \times 1000 \times M_{salt}} \tag{7}$$

where I (A) is the current at the operation time of t (min). ∫Idt can be obtained by integrating the corresponding current. $M_{salt}$ (58.44 g $mol^{-1}$) is the molecular mass of NaCl, while m (g) is the total mass of the two electrodes. F is the Faraday's constant (96,485 C $mol^{-1}$).

The energy consumption for desalination (EC, Wh/$m^{-3}$) by the CDI cell (pumping not considered) was calculated as follows [32]:

$$EC = \frac{\int UIdt}{V} \tag{8}$$

where U (V) is voltage.

## 3. Results and discussion

### 3.1. Physicochemical characterizations of NPC

#### 3.1.1. Crystal structure and surface morphology

The XRD patterns of NPC-x and CNPC samples are depicted in Fig. S1. The significant peaks at 26° and 44° are assigned to the (0 0 2) and (1 0 1) plane of the hexagonal graphite within NPC-x (JCPDS card no. 41–1487), respectively [33]. The presence of graphite carbon within NPC-x is considered as the source of electrical conductivity and thus helps to reduce the electron transfer impedance. The surface morphology of a typical NPC and CNPC samples are shown in Fig. 1 and Fig. S2. In general, NPC and CNPC possess uniform two-dimensional (2D) nanosheets. The thickness of nanosheets ranges from 50 nm to 100 nm. Meanwhile, the nanosheets present in their folded shape, which is favorable for fully exposing the active adsorption sites (Fig. 1b-c and Fig. S2a-c). We hypothesize that the folded structure is probably due to the graphitization of β-folded sheet proteins within silkworm cocoon [33,34]. Moreover, there exist many tiny pores on the surface of 2D nanosheets, which can be verified by the enlarged SEM images (Fig. 1d). We believe that such unique structural characteristics will help to reduce the diffusion resistance between electrode material and electrolyte while simultaneously shortening the ion diffusion distance to facilitate the charge-transfer reaction [35].

#### 3.1.2. Elemental composition and chemical state

The X-ray photoelectron spectroscopy (XPS) analysis was used to probe the elemental composition and chemical state of NPC-x and CNPC samples. As indicated in Fig. S3a and Table S1, NPC-x is *N*-containing carbonaceous materials. The content of N atoms within NPC-x samples decreased with an increase in the dosage of $ZnCl_2$, suggesting the negative role of high dosages of $ZnCl_2$ in forming nitrogen-rich NPC-x. Obviously, the effect of $ZnCl_2$ dosages on the contents of O atoms is not straightforward. However, we postulate that the co-presence of O and N would be favorable for generating defects within NPC-x [36]. The contents of N and O atoms within NPC-1.5 are comparable to those of CNPC (refer to Fig. S3b and Table S1). This verifies the selection of using SCW as the precursor to synthesize NPC rather than the pure silkworm cocoon. This is due to the fact that the main compositions of CW are silkworm chrysalis and abandoned silkworm cocoon (with protein content being up to 6,000 mg $L^{-1}$) [28]. The amino acids within SCW can serve as the intrinsic nitrogen source to form *N*-rich carbonaceous materials without using externally added nitrogen-containing chemicals. As shown in Fig. S3c, the water contact angles for NPC-x and CNPC (99° – 133.73°) were smaller than that of AC (147.38°). The water contact angles of NPC-x samples decreased with the increased contents of N atoms within NPC-x. The improved hydrophilicity of NPC-x can enhance the ion diffusion rate [24], thus improving the CDI performance.

The high-resolution N 1 s XPS spectra indicate the presence of different N species within NPC-x samples (Fig. 2a-e). Generally, the N species include oxidized-N (403.2 eV), graphitic-N (401.6 eV), pyrrolic-N (399.1 eV), and pyridinic-N (398.4 eV) for all the samples [36]. As shown in Fig. 2f and Table S2, the contents of both graphitic-N and oxidized-N species were firstly increased, and then decreased with the increased dosages of $ZnCl_2$, suggesting the negative effect of excessive $ZnCl_2$ on forming graphitic-/oxidized- N species. The lone pair electrons of nitrogen atoms within the structures of graphitic-N and oxidized-N may induce conjugation effect, which could enhance the electronic conductivity of NPC-x samples [38]. The fitted high-resolution C 1 s XPS spectra of NPC-x and CNPC were also provided in Fig. S4a-e. The peak at the binding energy of 284.6 eV is due to the presence of $sp^2$ hybridized carbon atoms [39]. Their relatively higher contents suggest that most of the C atoms within NPC-x and CNPC were arranged in conjugated honeycomb lattices, which derived from the aliphatic carbon of amino acids [40]. The peaks at 285.6 eV are assigned to the C—N bonds [41]. The relative contents of C—N bonds within NPC-0.5, NPC-1, NPC-1.5, NPC-2 and CNPC are 36.04 %, 30.37 %, 23.59 %, 19.60 % and 20.98 %, respectively, further confirming that nitrogen atoms were successfully doped into the porous carbon frameworks (Table S3). The presence of the peaks at 286.6 eV and 289.4 eV (corresponding to C—O and O═C-O, respectively) may result in better conductivity and hydrophilicity for NPC and CNPC [36]. ICP-OES tests indicate that the residual contents of Zn within NPC-x samples were less than 1 % (Table S4), and it was found that the residual Zn played insignificant role in the CDI desalination.

#### 3.1.3. Pore structure

According to the nitrogen adsorption–desorption isotherms (Fig. 3a), NPC-1.5, NPC-2 and CNPC have a type-IV curve with apparent hysteresis loops, which implies the formation of more abundant cage-type mesopores [42]. At the low relative pressure region ($P/P_0 < 0.1$), there exists significant nitrogen adsorption volume for NPC-1.5, NPC-2 and CNPC, indicating the presence of abundant micropores. The curves occurred at the middle relative pressure ($0.3 < P/P_0 < 0.8$) which reveals the existence of mesoporous, while a small amount of macropores can be verified by the slightly increased curves at the high relative pressure ($0.8 < P/P_0 < 1.0$). On the contrary, NPC-0.5 and NPC-1 show type-I curve as nitrogen adsorption balanced after $P/P_0 = 0.1$, implying that they possess a typical microporous structure. According to the BJH method, there is no significant difference between NPC-1.5 and CNPC in the mesopore range (2–20 nm), while they clearly show significant increase as compared to others as shown in Fig. 3b. It is accepted that abundant mesopores will provide effective pore volume for ion adsorption [43]. All the samples have the structural characteristics of micropore, mesopore and macropore, especially for NPC-1.5 and CNPC (Fig. S5), which is beneficial for the better utilization of their available sites during the CDI desalination process. The micropores of NPC-x and CNPC can provide high specific surface area and large number of adsorption sites to improve the double layer capacitance, while the mesopores can reduce the transport resistance of ions and the stacking of double electric layer [43]. The macropores acting as a buffer allow the ions to easily migrate to the interior surface of the electrode material,

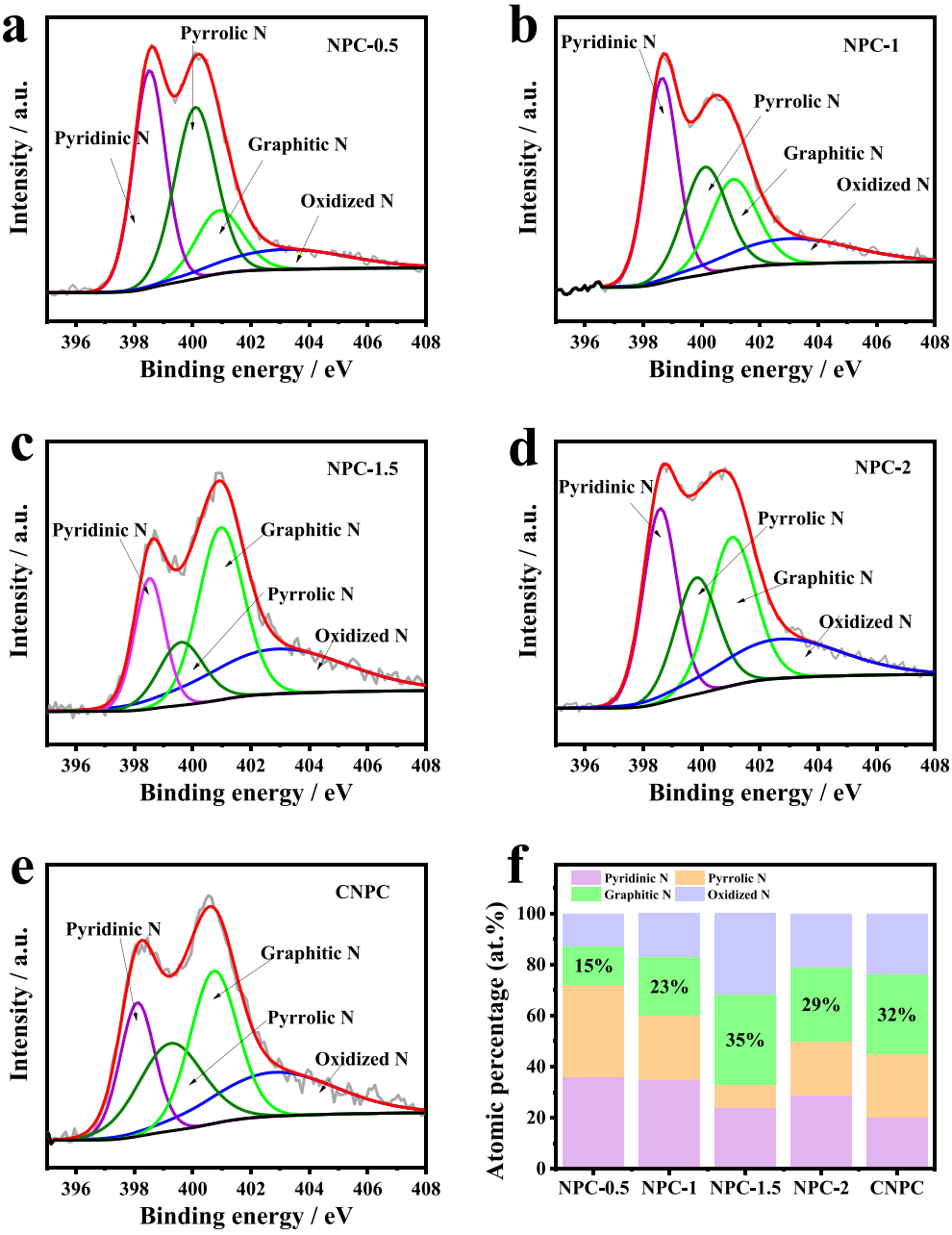


**Fig. 2.** High resolution N1s XPS spectra of NPC-0.5 (a), NPC-1 (b), NPC-1.5 (c), NPC-2 (d), and CNPC (e); and the atomic percentage of different N species (f).

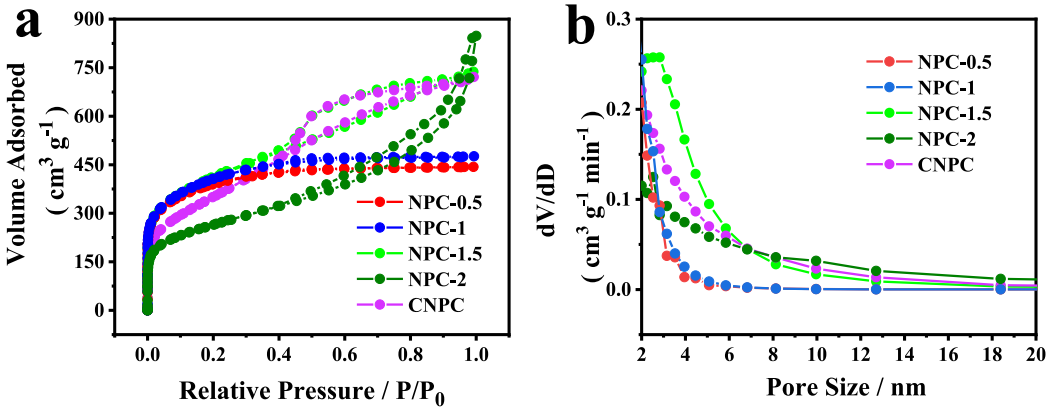


**Fig. 3.** Characterizations of the porous structures of NPC-x and CNPC: (a) nitrogen adsorption–desorption isotherms, (b) pore size distribution by BJH method.

thus speeding up the ion transport rates [44].

Table 1 summarizes the specific surface area and pore volume distribution. All samples have a high specific surface area ranging from 911 – 1409 $m^2/g$, which is conducive to the formation of double layer capacitance [33]. The specific surface areas of NPC-0.5, NPC-1, NPC-1.5, NPC-2 and CNPC are 1295, 1311, 1282, 911 and 1409 $m^2/g$, respectively. The lower BET values of NPC-1.5 and NPC-2 than those of NPC-0.5 and NPC-1 is due to the reduced micropore volume caused by the increase in $ZnCl_2$ concentration [45]. The average pore sizes for NPC-x were generally increased with the concentration of $ZnCl_2$ increased from 0.5 to 2 M, while the variation trend of pore volume ratio was similar to that of average pore size. In detail, the average pore sizes were gradually increased from 2.11 nm to 5.3 nm. The calculated pore volumes of NPC-0.5, NPC-1, NPC-1.5, and NPC-2 are 0.69, 0.74, 1.11, and 1.21 $cm^3\ g^{-1}$, respectively, while the corresponding mesoporous volume ratios are 26.73 %, 30.34 %, 75.47 %, and 69.09 %, respectively. Interestingly, the corresponding mesoporous ratios are firstly increased and then decreased. In summary, NPC-1.5 (75.47 %) possesses the largest mesoporous volume ratio compared with other samples. The NPC-x samples prepared at the lower concentration of $ZnCl_2$ are mainly composed of microporous, while the samples obtained from the lower concentration of $ZnCl_2$ possess mesoporous and macroporous structures simultaneously, especially for NPC-2 (Fig. 3 and Table 1). That is due to the gradually increased release of $CO_2$ and CO with the increase in the concentration of $ZnCl_2$, which can induce change of the micropores into mesopores and macropores [45]. It is accepted that the micropores within electrode materials will cause stacks of double electric layer, while the mesopores are favorable for the CDI desalination application due to the accelerated ion transport and the adsorption [46].

### 3.1.4. Raman spectra characteristics

The Raman spectra of NPC-x and CNPC are shown in Fig. 4a. The D band at 1350 $cm^{-1}$ is due to the $sp^2$ carbon atoms of NPC-x with defect structures, while the G band at 1545 $cm^{-1}$ is assigned to the $sp^3$ graphene carbon structure [33]. The high intensity ratios of $I_D/I_G$ values indicate the presence of abundant surface defects and high structure disorder. The $I_D/I_G$ value of NPC-1.5 (1.06) is higher than those of NPC-0.5 (0.86), NPC-1 (0.97), NPC-2 (0.99) and CNPC (1.01), indicating the abundant defects within NPC-1.5. It is noteworthy that the $I_D/I_G$ values are highly linear with the graphite-N content for all the samples (Fig. 4b). The existence of defects facilitates for the formation of adsorption sites, which will enhance the transport of ions and electrons in the adsorption process [36]. This was confirmed by the subsequent impedance tests (Fig. 5h).

## 3.2. Electrochemical characterization

It is known that the polarized porous carbon materials within the electrode could form an electric double layer (EDL) to store charge, which can attract opposite electrolyte ions on their surface, when it is polarized by an applied voltage [35]. Fig. 5a shows the CV curves of NPC-x, CNPC and AC at a scan rate of 10 mV $s^{-1}$. All the curves exhibit rectangular shape patterns without redox peaks, suggesting a character of typical double-layer capacitance. In particular, NPC-1.5 possesses the largest rectangular area than others, achieving the highest capacitance of 244.9 F/g. Fig. 5b shows the CV curves of NPC-1.5 under different scanning rates from 10 to 100 mv $s^{-1}$, while the CV curves of other samples at different scanning rates are given in Fig. S6a-e. Apart from the increasing trend of specific capacitance along with mesoporous rate, capacitance retention rate from 10 to 100 mV $s^{-1}$ was also investigated to reveal the effect of mesoporous (Fig. S7).

**Table 1**
Summary on the pore structural parameters of samples.

| Samples | $S_{BET}$ / $m^2/g$ | Mean pore size / nm | $V_{total}$ / $cm^3\ g^{-1}$ | $V_{micro}$ / $V_{total}$ | $V_{meso}$ / $V_{total}$ | $V_{macro}$ / $V_{total}$ |
|---|---|---|---|---|---|---|
| NPC-0.5 | 1295 | 2.11 | 0.69 | 73.07 % | 26.73 % | 0.2 % |
| NPC-1 | 1311 | 2.16 | 0.74 | 69.49 % | 30.34 % | 0.17 % |
| NPC-1.5 | 1282 | 3.5 | 1.11 | 23.11 % | 75.47 % | 1.42 % |
| NPC-2 | 911 | 5.3 | 1.21 | 16.08 % | 69.09 % | 14.83 % |
| CNPC | 1409 | 3.2 | 1.14 | 31.03 % | 62.70 % | 6.27 % |

The GCD curves of NPC-x and CNPC electrodes at a high current density (1 A/g) are depicted in Fig. 5c. All the curves display the symmetric triangular shapes, demonstrating an ideal electrical double-layer capacitor behavior and good electrochemical reversibility. The longest discharge time of NPC-1.5 means the largest specific capacitance. It is found that the specific capacitances for all the samples followed the same order for the ratios of graphitic-N and mesopores, i.e., NPC-0.5 (155.06 F/g) < NPC-1 (170.51 F/g) < NPC-2 (188.90 F/g) < CNPC (214.70 F/g) < NPC-1.5 (244.9 F/g).

Fig. 5d shows that the specific capacitances for all the samples decreased with the increased scan rate. The NPC-1.5 shows the highest specific capacitance regardless of the scan rates. The high specific capacitance of NPC-1.5 is conducive to the CDI related applications. Meanwhile, the diffusion capacitance and surface capacitance were quantified by a pre-established method by Trasatti [47]. The surface capacitance can be calculated by the extrapolation of CV curves at high scan rates, while the total capacitance could be obtained by the same method at lower scan rates (refer to Fig. 5e and f). The surface capacitance contributions of NPC-0.5, NPC-1, NPC-1.5, NPC-2, CNPC and AC are 66 %, 69 %, 74 %, 71 %, 72 % and 43 %, respectively (Fig. 5g), suggesting a typical capacitive-controlled capacitance process for CDI desalination application.

The EIS was used to investigate the electrical resistance and charge transport behavior of NPC-x and CNPC samples (Fig. 5h). In the high-frequency region, the value of bulk resistance ($R_s$) was obtained by the x-intercept. Obviously, the $R_s$ values of NPC-1.5 and CNPC are smaller than others, demonstrating their lower intrinsic resistance and superior conductivity. The relatively low $R_s$ of NPC-1.5 and CNPC electrodes was apparently attributed to the higher specific surface area and the larger mesoporous volume ratio. It is accepted that the mesopores can reduce the transport resistance of ions [43]. The ions at the interface between the electrode and electrolyte can facilitate the transport and accumulation. However, $R_s$ value of NPC-0.5 is high than that of AC, mainly due to the lower specific surface area of NPC-0.5 than that of AC (Table S6). The charge transfer resistance ($R_{ct}$) occurred at the electrode/electrolyte interface can be obtained by the diameter of the quasi-semicircle in the high-frequency region. The $R_{ct}$ values of NPC-0.5, NPC-1, NPC-1.5, NPC-2, CNPC and AC are 2.45, 2.09, 0.97, 1.82, 0.89 and 2.98 Ω, respectively (Table S5). The lower $R_{ct}$ values of NPC-1.5 and CNPC electrodes further confirm their excellent conductivity. It is noteworthy that the $R_{ct}$ values are highly linear with the graphite-N contents for all the samples (Fig. S6f). This is due to the improved conductivity of carbon materials caused by the increased contents of graphite-N species [38].

The Nyquist plots at the low frequency region are widely used to reveal the Warburg diffusion process for CDI desalination [24]. By fitting the Nyquist plots and using the equations of (3) and (4), the ion diffusion coefficient ($D_{Na+}$) of the electrodes can be obtained. As shown in Fig. 5i, NPC-1.5 and CNPC exhibit larger $D_{Na+}$ values ($1.23x10^{-14}$ $cm^2\ s^{-1}$ and $9.23x10^{-15}$ $cm^2\ s^{-1}$) than NPC-0.5 ($4.5x10^{-15}$ $cm^2\ s^{-1}$), NPC-1 ($5.41x10^{-15}$ $cm^2\ s^{-1}$), NPC-2 ($7.15x10^{-15}$ $cm^2\ s^{-1}$) and AC ($1.5x10^{-15}$ $cm^2\ s^{-1}$). This suggests that the NPC-1.5 and CNPC electrodes possess low ionic diffusion resistance, which is conducive to the CDI desalination application.

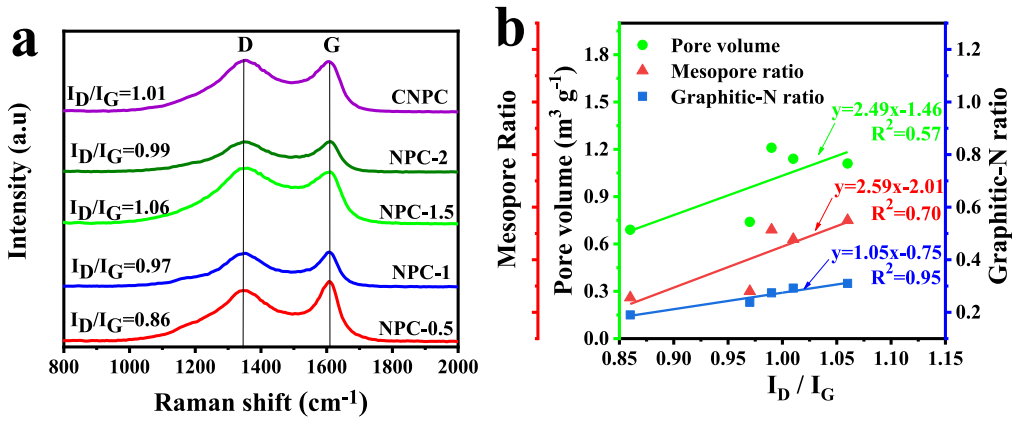


**Fig. 4.** (a) Raman spectra of NPC-x and CNPC, (b) the relationships between the $I_D/I_G$ values and the graphite-N ratio, mesoporous ratio and pore volume.

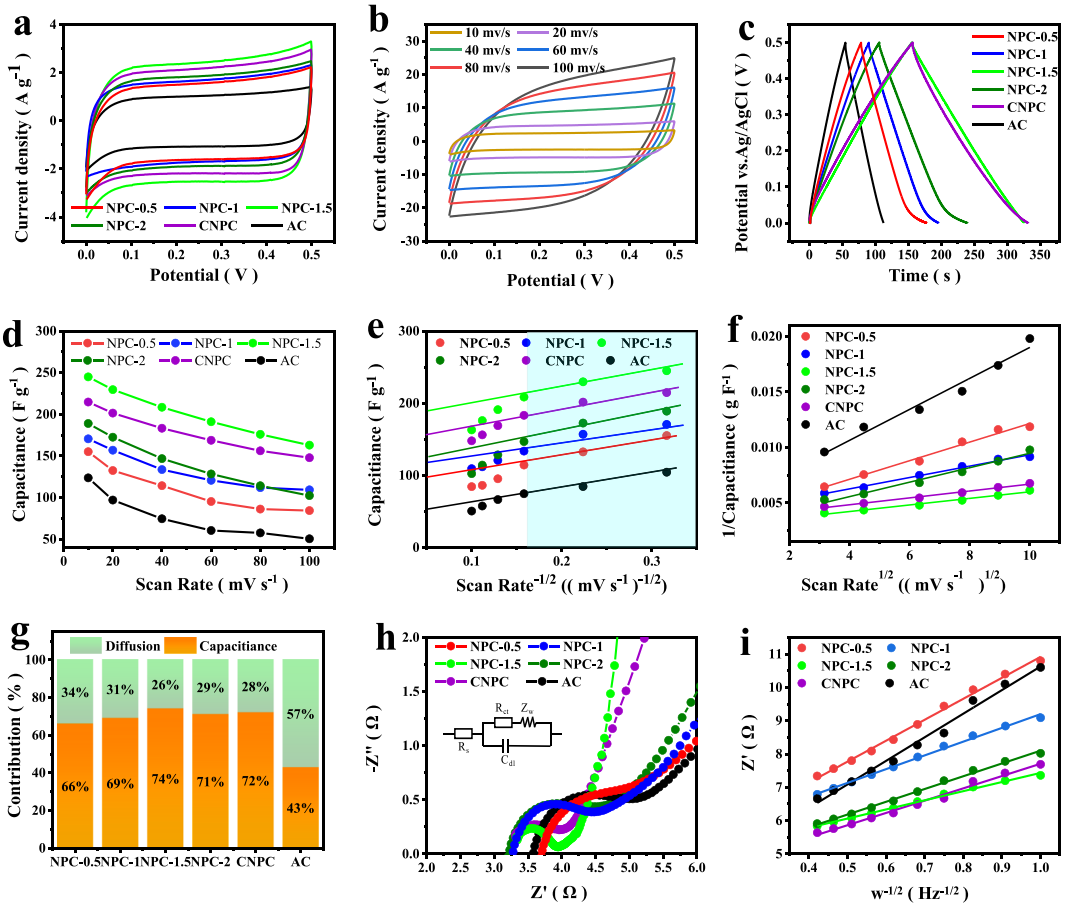


**Fig. 5.** Electrochemical properties of NPC-x, CNPC and AC-based electrodes. (a) CV curves at a scan rate of 10 mV $s^{-1}$ and (b) CV curves of NPC-1.5 at different scan rates, (c) GCD curves at a current density of 1 A/g in 1 M NaCl solution, (d) the capacitance at various scan rates, (e) the relationship between the specific capacitance and inverse square root of scan rate, and (f) the relationship between the inverse specific capacity and square root of scan rate, (g) the capacitance contribution analysis, (h) EIS results, (i) Zreal vs reciprocal of the square root of frequency (ω) for the electrodes and the resulting $Na^+$ diffusion coefficients determined from EIS of the electrode materials.

### *3.3. Desalination performance and mechanism*

#### *3.3.1. NPC-x characteristics-regulated desalination process*

Various electrodes were prepared with NPC-x, CNPC and AC for CDI process to assess their desalination performance. As depicted in Fig. S8a, the electrical conductivity of 100 mg $L^{-1}$ NaCl solution barely decresed without electricity charging, indicating the weak physical and chemical adsorption of NPC-1.5 electrode for Na + and Cl- ions. However, according to Fig. 6a, in the first five minutes, the electrical conductivity of all the solutions decreased significantly. This is due to the rapid formation of the EDL [48]. As shown in Fig. 6b, NPC-1.5 demonstrates the highest desalination capacity. In detail, the desalination capacities of NPC-0.5, NPC-1, NPC-1.5, NPC-2, CNPC, and AC at the time of 20 min are 13.43, 15.00, 22.19, 16.88, 20.93, and 10.94 mg $g^{-1}$, respectively. It is generally believed that carbon materials with large specific surface area and a large number of desired pores will achieve high desalination

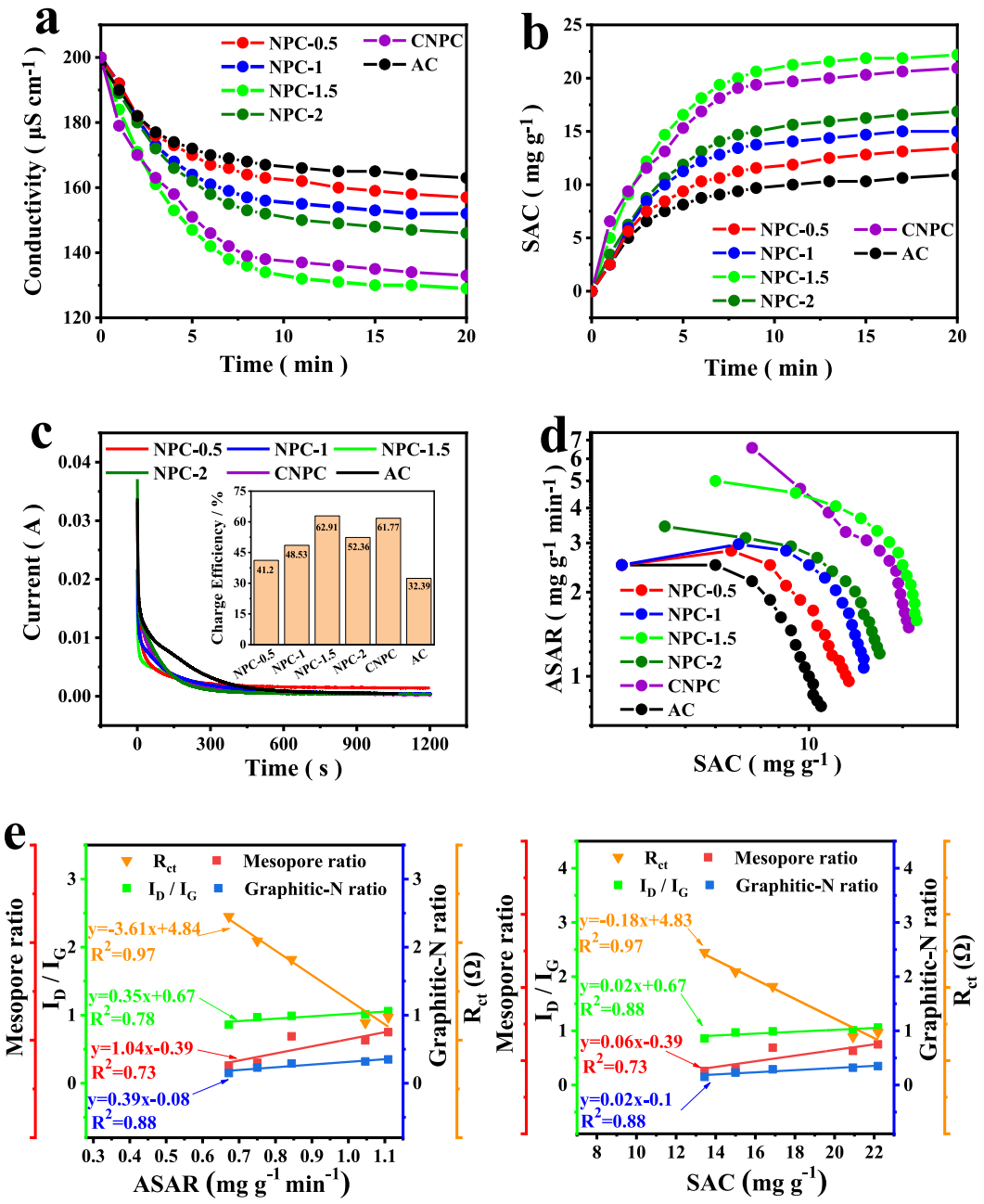


**Fig. 6.** The CDI desalination performance of the NPC-x, CNPC and AC-based electrodes. (a) The conductivity changes of 100 mg $L^{-1}$ NaCl solution with 1.2 V at the flow rate of 40 mL $min^{-1}$, (b) CDI desalination capacity, (c) the current response and corresponding charge efficiency, (d) Ragone plots, (e) the linear relationships between ASAR and the $I_D/I_G$ value, mesoporous ratio, graphite-N and $R_{ct}$ value, and (f) the linear relationships between SAC and the $I_D/I_G$ value, mesoporous ratio, graphite-N and $R_{ct}$ value.

capacity. Interestingly, NPC-1.5 and CNPC have high desalination capacities due to higher proportion of mesoporous as effective storage layers for salt ions, although with lower specific surface area. Furthermore, the defects caused by the presence of graphitic-N create additional active sites for $Na^+$ and $Cl^-$ storage [10]. The higher desalination capacity of NPC-x electrodes than that of AC suggests the superiority of using waste silkworm cocoon to fabricate *N*-doped CDI electrodes. The CDI desalination performance of NPC-1.5 is comparable to that of CNPC, suggesting the feasibility of using SCWs as the starting materials to prepare the CDI electrodes. Moreover, the SAC of NPC-1.5 can be increased to 34.68 mg $g^{-1}$ by using a pair of cation exchange membranes to form an integrated MCDI (Fig. S8b).

Fig. 6c shows the current responses and the corresponding charge efficiencies of all the carbonaceous electrodes. The charge efficiencies values of NPC-0.5, NPC-1, NPC-1.5, NPC-2, CNPC, and AC electrodes are 41.20 %, 48.53 %, 62.91 %, 52.36 %, 61.77 %, and 32.39 %, respectively. It is accepted that, the higher the charge efficiency of one electrode is, the lower is the energy consumption of its desalination application [48]. According to the formula 8, the energy consumption of NPC-0.5, NPC-1, NPC-1.5, NPC-2, CNPC, and AC electrodes were calculated to be 64.95, 50.02, 45.66, 47.07, 46.85, and 74.03 Wh/$m^{-3}$, respectively (Fig. S8c). Therefore, it is understandable that NPC-1.5 has the best desalination performance among all the electrodes. Note that all charge efficiencies for the NPC-x electrodes are less than 100 %. This is due to the combined effects of co-ionic effects, the impedance of the binder within electrode, and the contact resistance between the electrode and the collector [37]. However, this problem can be alleviated via a MCDI process (Fig. S8d,e), and its charge efficiency can be increased to

98.44 % (with an energy consumption of 33.20 Wh/$m^{-3}$).

The Ragone plots were used to further probe the desalination performance of electrodes (Fig. 6d). Usually, the higher SAC and ASAR values obtained from the plots indicate a higher electrosorption capacity and faster electrosorption rate for the electrodes used in the CDI desalination process [49]. Apparently, the average adsorption rates of NPC-1.5 and CNPC are significantly higher than others, agreeing well with the findings from the current response and charge efficiencies. As shown in Fig. 6e and 6f, both the ASAR and SAC values are highly linear with the $R_{ct}$ values ($R^2 = 0.97$), but poorly linear with the mesoporous ratios ($R^2 = 0.75$). This suggests that the $R_{ct}$ is a critical factor dominating the desalination performance of NPC-x. Lowering the $R_{ct}$ value and increasing the mesoporous ratio of electrode materials are conducive to improving their desalination efficacy. This is due to the fact that: i) Lowering the $R_{ct}$ value will reduce the electrochemical polarization of electrode; ii) Increasing the mesoporous ratio will reduce the ion transport resistance and the stacking of EDL on the electrode surface, thus provide effective specific surface for ion adsorption [2]. Benefiting from the synergistic effect of mesoporous and $R_{ct}$, NPC-1.5 represents superior desalination capacity.

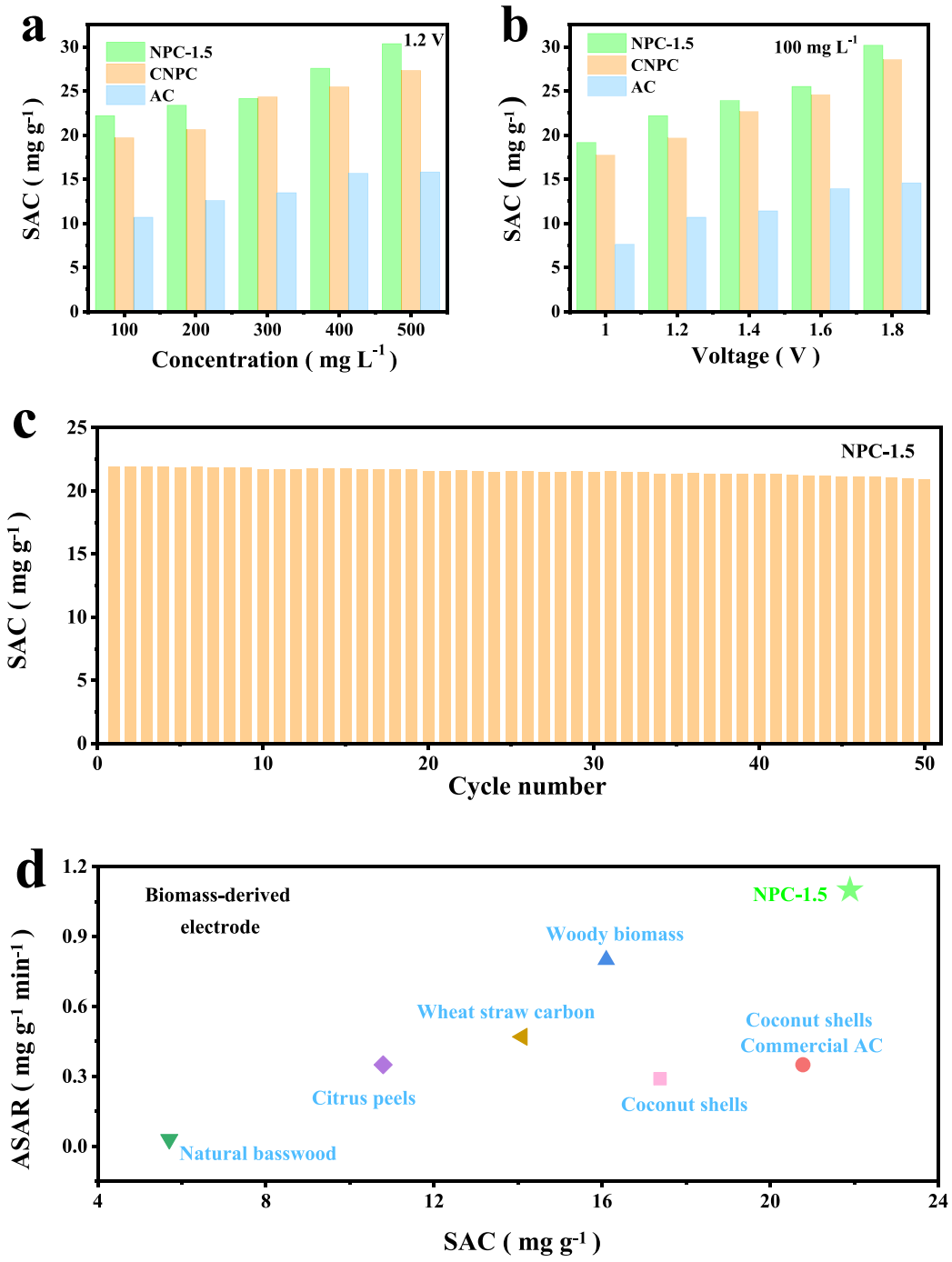


**Fig. 7.** The CDI desalination capacity of NPC-1.5, CNPC and AC under different NaCl solution concentrations (a) and different applied voltages (b), the stability of NPC-1.5 electrode during 50 successive CDI desalination cycles (c), comparison of CDI desalination performance of NPC-1.5 with the recently reported biomass carbon-based electrodes (The details are shown in Table S7) (d).

### 3.3.2. Operating parameters-regulated CDI desalination

The optimized NPC-x was used to further probe the effects of initial NaCl concentration and applied voltage on its CDI desalination performance. The CDI performance at different initial NaCl concentrations and a fixed applied voltage of 1.2 V is shown in Fig. 7a. With the initial NaCl concentration increased, the CDI desalination capacity for NPC-1.5, CNPC and AC-based electrodes increased. The SAC values of the NPC-1.5 electrode at NaCl concentrations of 100, 200, 300, 400, and 500 mg $L^{-1}$ are 22.19, 23.38, 24.14, 27.56, and 30.35 mg $g^{-1}$, respectively. This is due to improved ion transfer rate and reduced overlap effect at higher salt concentrations.

Clearly, the SAC values for NPC-1.5, CNPC and AC-based electrodes at a fixed initial NaCl concentration of 100 mg $L^{-1}$ show an upward trend with the increase of applied voltage (Fig. 7b). The higher applied voltage would result in a thicker EDL and stronger Coulombic interaction between salt ions and electrode, thus enhancing the electrosorption capacity. In detail, the SAC values of the NPC-1.5 electrode at the applied voltage of 1.0, 1.2, 1.4, 1.6, and 1.8 V are 19.16, 22.19, 23.93, 25.5, and 30.18 mg $g^{-1}$, respectively. These values are much higher than those of the AC electrode at the same voltage, further confirming the superiority of hierarchical NPC-x in CDI desalination application. The higher SAC values of NPC-1.5 than CNPC is due to the higher mesoporous ratio and lower $R_{ct}$ (refer to Table 1 and Table S5).

### 3.3.3. Reusability of NPC

The optimal NPC-1.5 was used as a model of NPC-x to study the reusability and long-term performance of the electrode materials over the 50-cycle desalination applications (Fig. 7c). Once each adsorption desalination process was finished, a followed procedure of short-circuit was employed to start the desorption of NaCl from the saturated electrode (20 min charging and 10 min discharging for each cycle). It is clear that the NPC-1.5 exhibited robust CDI desalination performance. In

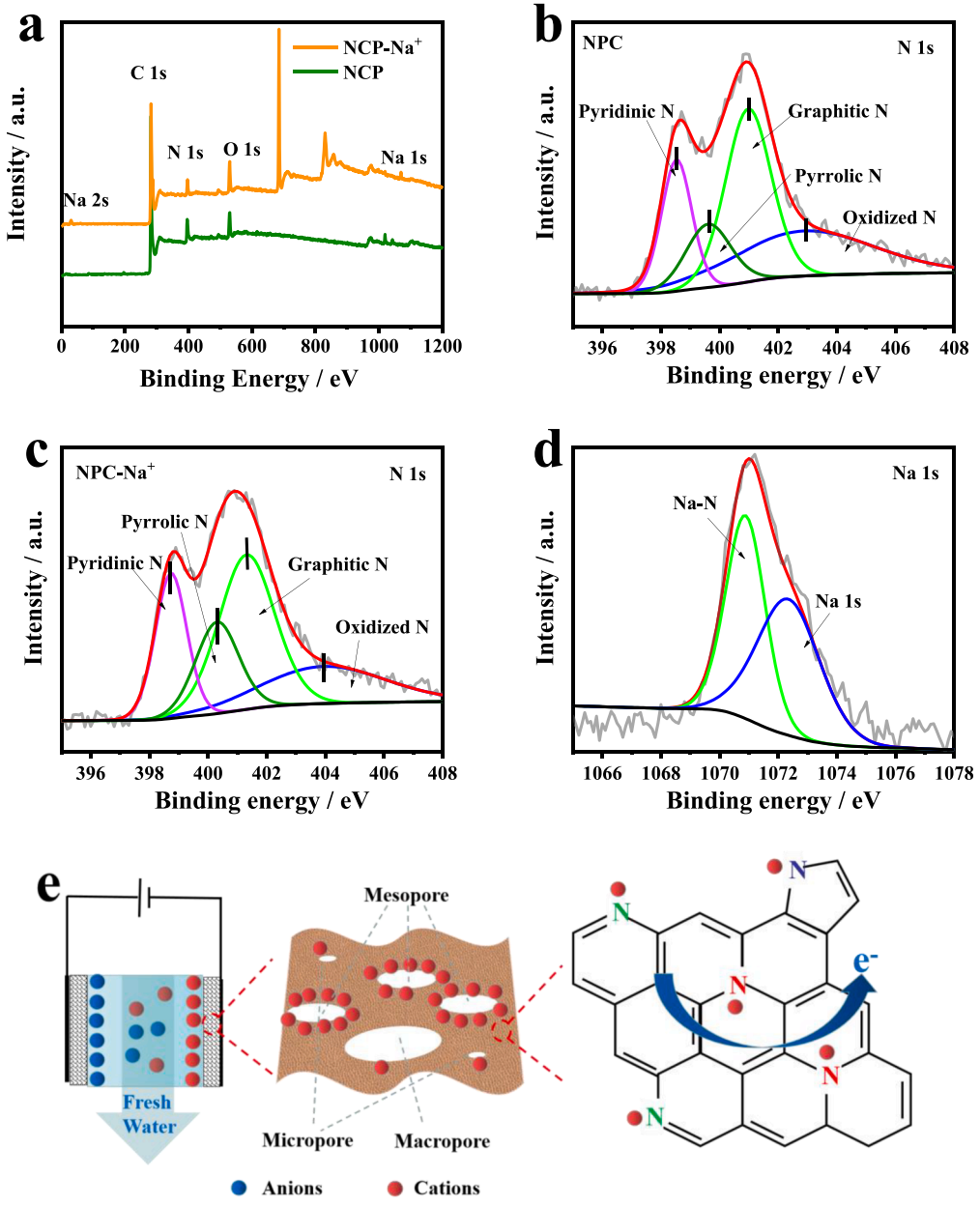


**Fig. 8.** Full-range XPS spectra of NPC-1.5 electrodes before (the bottom) and after (the top) CDI desalination in in 100 mg $L^{-1}$ NaCl solution (a), (b) high-resolution N 1 s XPS spectrum for fresh (b) and used (c) NPC-1.5 electrode, (d) high-resolution Na 1 s XPS spectrum for used NPC-1.5 electrode, and the schematic illustration on the CDI desalination of NPC-1.5 electrode (e).

particular, the electrosorption capacity of NPC-1.5 after 50 cycles can still be above 21.52 mg $g^{-1}$. Compared with the fresh NPC-1.5 (22.19 mg $g^{-1}$), the rate for the decreased desalination capacity of used NPC-1.5 in the 50th cycle is less than 3 %. These results suggest the excellent reusability and stability of NPC-x.

In addition, we summarized the desalination capacities of some other biomass-based electrodes to further exhibit the superiority of the optimized NPC-x. It is obvious that, the desalination ability of NPC-1.5 is superior to those of recently reported biomass-derived carbon electrodes [17,50–55], as well as those of commercial activated carbon, carbon cloth and graphene (Fig. 7d and Table S7) [53–59]. The average desalination rate of NPC-x is as high as 1.1 mg $g^{-1}$ $min^{-1}$, more than 2 times higher than those of biomass-derived carbon electrodes (usually below 0.5 mg $g^{-1}$ $min^{-1}$) [17,50–55]. These findings imply the superiority of NPC-x in the CDI desalination application, thus suggesting the feasibility of using waste silkworm cocoon as the precursors of CDI electrodes.

### 3.3.4. Desalination mechanism of NPC

The NPC-1.5 electrodes before and after CDI process were used to probe the desalination mechanism. Compared with the fresh NPC-1.5 electrode, the signal peak of Na 1 s was observed in the used NPC-1.5 electrode (Fig. 8a), confirming the successful electrosorption of $Na^+$ by the electrodes. After the CDI desalination application, the binding energy peaks of oxidized-N, graphitic-N, pyrrolic-N, and pyridinic-N with the NPC-1.5 electrode were increased by 0.86, 0.13 0.42, and 0.49 eV, respectively (Fig. 8b, c). This suggests that the different N species within NPC-1.5 have a strong affinity with $Na^+$ ions, thus enhancing the binding energy. We also can find the two peaks at 1071.76 eV and 1070.8 eV for Na 1 s, which are suggested to the metal Na and N complexed Na, respectively products (Fig. 8d) [60]. For the C 1 s of used NPC-1.5 electrode, the C—N bond at 285.3 eV was shifted to 285.1 eV (Fig. S9a, b). The decrease of binding energy could be explained by the changed chemical environment of C atoms [61]. Another reason is the formation of Na-N over the desalination process, which increased the density of electron cloud around C atom in C—N—Na and thus reduced the binding energy.

It is known that the electrochemically active nitrogen atoms (especially pyrrolic-N and pyridinic-N) could control the local electronic structures and the defects of electrode materials, which is beneficial to the CDI-based electrosorption of $Na^+$ ions from the solution [62]. Besides, the graphitic nitrogen atoms can enhance the CDI-based electrosorption capacity by improving the electrical conductivity of the electrode materials (responsible for the electron transport within the electrode) [62]. As revealed by the CV tests in the aqueous NaCl solutions (Fig. 5g), the diffusion-controlled process also accounted for the CDI-based electrosorption of $Na^+$ ions. Hence, we think that the outstanding CDI desalination efficiency of NPC-1.5 electrode can be attributed to the synergistic processes of the defects dominated-capacitance caused by different N species and electro-adsorption induced by the electrochemical double layer formation across the porous carbon nanosheets (as show in Fig. 8e).

## 4. Conclusions

In summary, this is a study for the first time of using waste silkworm cocoon as the precursor for the synthesis of CDI electrode for the desalination application. The nitrogen contents, defect densities, and pore structures of silkworm cocoon-derived NPC-x can be simply tuned by the concentration of $ZnCl_2$. The resultant NPC-x with more defects and mesoporous structure exhibited higher electrical conductivity and lower ion diffusion resistance. The electrosorption capacity for NaCl linearly correlated with the defect densities of NPC-x (i.e., the $I_D/I_G$ values). The optimized NPC-1.5 possesses an electrosorption capacity of 21.9 mg $g^{-1}$ with an average desalination rate of 1.1 mg $g^{-1}$ $min^{-1}$, much higher than those of the most commonly used carbonaceous electrodes (including the activated carbon-based ones). Moreover, the optimized NPC-1.5 is quite stable and robust in the long-term CDI desalination application over 50 successive charge–discharge cycles, thus demonstrating a potential of using waste silkworm cocoon-derived CDI electrode devices in the desalination of seawater/brine. Results from this work will spark more interests on utilizing the carbon/nitrogen-rich wastes/biomasses to design versatile carbonaceous devices for wastewater purification via more sustainable and environmentally friendly routes.

## Declaration of Competing Interest

The authors declare that they have no known competing financial interests or personal relationships that could have appeared to influence the work reported in this paper.

## Data availability

Data will be made available on request.

## Acknowledgements

We acknowledge the funding supports from the National Natural Science Foundation of China (No. 51978639), the Youth Innovation Promotion Association CAS (2019307), the Natural Science Foundation of Fujian Province (No. 2020J01120) and Chemistry and Chemical Engineering Guangdong Laboratory (No. 1912005). D. D. Dionysiou also acknowledges support from the University of Cincinnati through the Herman Schneider Professorship in the College of Engineering and Applied Sciences.

## Appendix A. Supplementary data

Supplementary data to this article can be found online at https://doi.org/10.1016/j.cej.2023.141471.

## References

[1] Y. Liu, K. Wang, X.T. Xu, K. Eid, A.M. Abdullah, L.K. Pan, Y. Yamauchi, Recent advances in faradic electrochemical deionization: system architectures versus electrode materials, ACS Nano 15 (9) (2021) 13924–13942, https://doi.org/10.1021/acsnano.1c03417.

[2] M.E. Suss, S. Porada, X. Sun, P.M. Biesheuvel, J. Yoon, V. Presser, Water desalination via capacitive deionization: what is it and what can we expect from it? Energ. Environ. Sci. 8 (8) (2015) 2296–2319, https://doi.org/10.1039/c5ee00519a.

[3] K. Singh, G.N. Li, J. Lee, H. Zuilhof, B.L. Mehdi, R.L. Zornitta, L.C.P.M. de Smet, Divalent ion selectivity in capacitive deionization with vanadium hexacyanoferrate: experiments and quantum-chemical computations, Adv. Funct. Mater. 31 (41) (2021) 2105203, https://doi.org/10.1002/adfm.202105203.

[4] R. Uwayid, E.N. Guyes, A.N. Shocron, J. Gilron, M. Elimelech, M.E. Suss, Perfect divalent cation selectivity with capacitive deionization, Water Res. 210 (2022), 117959, https://doi.org/10.1016/j.watres.2021.117959.

[5] J.G. Gamaethiralalage, K. Singh, S. Sahin, J. Yoon, M. Elimelech, M.E. Suss, P. Liang, P.M. Biesheuvel, R.L. Zornitta, L.C.P.M. de Smet, Recent advances in ion selectivity with capacitive deionization, Energ. Environ. Sci. 14 (3) (2021) 1095–1120, https://doi.org/10.1039/D0EE03145C.

[6] A.N. Shocrona, E.N. Guyesa, H.H.M. Rijnaartsb, P.M. Biesheuvelc, M.E. Sussa, J. E. Dykstra, Electrochemical removal of amphoteric ions, Proc. Natl. Acad. Sci. 118 (40) (2021), https://doi.org/10.1073/pnas.2108240118.

[7] L. Shi, E. Newcomer, M. Son, V. Pothanamkandathil, C.A. Gorski, A. Galal, B. E. Logan, Metal-ion depletion impacts the dtability and performance of battery electrode deionization over multiple cycles, Environ. Sci. Technol. 55 (8) (2021) 5412–5421, https://doi.org/10.1021/acs.est.0c08629.

[8] Y.C. Xiong, F. Yu, S. Arnold, L. Wang, V. Presser, Y.F. Ren, J. Ma, Three-dimensional cobalt hydroxide hollow cube/vertical nanosheets with high desalination capacity and long-term performance stability in capacitive deionization, Research 49 (2021) 9754145, https://doi.org/10.34133/2021/9754145.

[9] W.H. Shi, X.Y. Liu, T.Q. Deng, S.Z. Huang, M. Ding, X.H. Miao, C.Z. Zhu, Y.H. Zhu, W.X. Liu, F.F. Wu, C.J. Gao, S.W. Yang, H.Y. Yang, J.N. Shen, X.H. Cao, Enabling superior sodium capture for efficient water desalination by a tubular polyaniline decorated with prussian blue nanocrystals, Adv. Mater. 32 (33) (2020) 1907404, https://doi.org/10.1002/adma.2019,07404.

[10] J.J. Lei, Y.C. Xiong, F. Yu, J. Ma, Flexible self-supporting CoFe-LDH/MXene film as achloride ions storage electrode in capacitive deionization, Chem. Eng. J. 437 (2022), 135381, https://doi.org/10.1016/j.cej.2022,135381.
[11] Q. Li, X.T. Xu, J.R. Guo, J.P. Hill, H.S. Xu, L.X. Xiang, C. Li, Y. Yamauchi, Y.Y. Mai, Two-dimensional MXene-polymer heterostructure with ordered in-plane mesochannels for high-performance capacitive deionization, Angew. Chem. Int. Ed. 60 (2021) 26528–26534, https://doi.org/10.1002/anie.202111823.
[12] Z.Q. Chen, Z.B. Ding, Y.Y. Chen, X.T. Xu, Y. Liu, T. Lu, L.K. Pan, Three-dimensional charge transfer pathway in close-packed nickel hexacyanoferrate−on−MXene nano-stacking for high-performance capacitive deionization, Chem. Eng. J. 452 (2023), 139451, https://doi.org/10.1016/j.cej.2022.139451.
[13] B. Han, G. Cheng, Y. Wang, X. Wang, Structure and functionality design of novel carbon and faradaic electrode materials for high-performance capacitive deionization, Chem. Eng. J. 360 (2019) 364–384, https://doi.org/10.1016/j.cej.2018,11,236.
[14] Y. Liu, X. Gao, K. Wang, X.Y. Dou, H.G. Zhu, X. Yuan, L.K. Pan, Rocking-chair capacitive deionization with flow-through electrodes, J. Mater. Chem. A 8 (2020) 8476–8484, https://doi.org/10.1039/C9TA14112J.
[15] X.T. Xu, L.K. Pan, Y. Liu, T. Lu, Z. Sun, Enhanced capacitive deionization performance of graphene by nitrogen doping, J Colloid Interface Sci. 445 (2015) 143–150, https://doi.org/10.1016/j.jcis.2015.01.003.
[16] X.T. Xu, S.H. Zhang, J. Tang, L.K. Pan, M. Eguchi, J. Na, Y. Yamauchi, Nitrogen-doped nanostructured carbons: A new material horizon for water desalination by capacitive deionization, Energy Chem. 2 (5) (2020), 100043, https://doi.org/10.1016/j.enchem.2020.100043.
[17] J.Y. Luo, D.C. Tian, Z.B. Ding, T. Lu, X.T. Xu, L.K. Pan, Enhanced cycling stability of capacitive deionization via effectively inhibiting $H_2O_2$ formation: The role of nitrogen dopants, Electroanal. Chem. 855 (2019), 113488, https://doi.org/10.1016/j.jelechem.2019.113488.
[18] X.T. Xu, J. Tang, Y.V. Kaneti, H.B. Tan, T. Chen, L.K. Pan, T. Yang, Y. Bando, Y. Yamauchi, Unprecedented capacitive deionization performance of interconnected iron–nitrogen-doped carbon tubes in oxygenated saline water, Mater. Horiz. 7 (5) (2020) 1404–1412, https://doi.org/10.1039/C9MH01829H.
[19] X.T. Xu, T. Yang, Q.W. Zhang, W. Xia, Z.B. Ding, K. Eid, A.M. Abdullah, M.S. A. Hossain, S.H. Zhang, J. Tang, L.K. Pan, Y. Yamauchi, Ultrahigh capacitive deionization performance by 3D interconnected MOF-derived nitrogen-doped carbon tubes, Chem. Eng. J. 390 (2020), 124493, https://doi.org/10.1016/j.cej.2020.124493.
[20] X.H. Liu, S.H. Zhang, G.L. Feng, Z.G. Wu, D. Wang, M.D. Albaqami, B. Zhong, Y. Chen, X.D. Guo, X.T. Xu, Y. Yamauchi, Core−shell MOF@COF motif hybridization: selectively functionalized precursors for titanium dioxide nanoparticle embedded nitrogen-rich carbon architectures with superior capacitive seionization performance, Chem. Mater. 33 (5) (2021) 1657–1666, https://doi.org/10.1021/acs.chemmater.0c04129.
[21] B.Q. Cen, K.X. Li, R. Yang, Expeditious and effectual capacitive deionization performance by chitosan-based carbon with hierarchical porosity, Desalination 531 (2022), 115703, https://doi.org/10.1016/j.desal.2022,115703.
[22] Y. Zhang, J.Y. Wu, S.H. Zhang, N.Z. Shang, X.X. Zhao, S.M. Alshehri, T. Ahamad, Y. Yamauchi, X.T. Xu, Y. Bando, MOF-on-MOF nanoarchitectures for selectively functionalized nitrogen-doped carbon-graphitic carbon/carbon nanotubes heterostructure with high capacitive deionization performance, Nano Energy 97 (2022), 107146, https://doi.org/10.1016/j.nanoen.2022.107146.
[23] Y. Li, J. Kim, J. Wang, N.L. Liu, Y. Bando, A.A. Alshehri, Y. Yamauchi, C.H. Hou, K.-C.-W. Wu, High performance capacitive deionization using modified ZIF-8-derived, N-doped porous carbon with improved conductivity, Nanoscale 10 (4) (2018) 14852, https://doi.org/10.1039/C8NR02288G.
[24] J. Chen, K.C. Zuo, B. Li, J.H. Hu, W.B. Liu, D.S. Xia, L. Lin, J.J. Liang, X.Y. Li, Fungal hypha-derived freestanding porous carbon pad as a high-capacity electrode for water desalination in membrane capacitive deionization, Chem. Eng. J. 433 (2022), 133781, https://doi.org/10.1016/j.cej.2021.133781.
[25] C. Zhao, Q. Wang, S. Chang, S. Zhang, Z. Li, Z. Shen, X. Jin, H. Xiao, H. Zhang, Efficient transport system of cultivated mushroom mycelium enables its derived carbon with High performance electrochemical desalination capability, Carbon 27 (2022), https://doi.org/10.1016/j.carbon.2022.05.020.
[26] J. Chen, K.C. Zuo, Y.L. Li, X.C. Huang, J.H. Hu, Y. Yang, W.P. Wang, L. Chen, A. Jain, R. Verduzco, X.Y. Li, Q.L. Li, Eggshell membrane derived nitrogen rich porous carbon for selective electrosorption of nitrate from water, Water Res. 216 (2022), 118351, https://doi.org/10.1016/j.watres.2022.118351.
[27] J.H. Hou, C.B. Cao, F. Idrees, X.L. Ma, Hierarchical porous nitrogen-doped carbon nanosheets derived from silk for ultrahigh-capacity battery anodes and supercapacitors, ACS Nano 9 (2015) 2556–2564, https://doi.org/10.1021/nn506394r.
[28] G. Capar, S.S. Aygun, M.R. Gecit, Separation of sericin from fatty acids towards its recovery from silk degumming wastewaters, J. Membr. Sci. 342 (2009) 179–189, https://doi.org/10.1016/j.memsci.2009.06.039.
[29] G. Capar, S.S. Aygun, M.R. Gecit, Treatment of silk production wastewaters by membrane processes for sericin recovery, J. Membr. Sci. 325 (2008) 920–931, https://doi.org/10.1016/j.memsci.2008.09.020.
[30] H.B. Li, W.Y. Shi, W. Wang, H.Y. Zhu, The extraction of sericin protein from silk reeling wastewater by hollow fiber nanofiltration membrane integrated process, Sep. Purif. Technol. 146 (2015) 342–350, https://doi.org/10.1016/j.seppur.2015.04.004.
[31] H.O. Li, T. Lu, L.K. Pan, Y.P. Zhang, Z. Sun, Electrosorption behavior of graphene in NaCl solutions, J. Mater. Chem. A 37 (2009) 6773–6779, https://doi.org/10.1039/B907703K.
[32] S.A. Hawks, A. Ramachandran, S. Porada, P.G. Campbel, M.E. Suss, P. M. Biesheuvel, J.G. Santiago, M. Stadermann, Performance metrics for the objective assessment of capacitive deionization systems, Water Res. 152 (2019) 126–137, https://doi.org/10.1016/j.watres.2018.10.074.
[33] X.R. Liu, M. Zhang, D.N. Yua, T. Li, M. Wan, H. Zhua, M.L. Du, J.M. Yao, Functional materials from nature: honeycomb-like carbon nanosheets derived from silk cocoon as excellent electrocatalysts for hydrogen evolution reaction, Electrochim. Acta 215 (2016) 223–230, https://doi.org/10.1016/j.electacta.2016.08.091.
[34] M.W. Xiang, Y. Wang, J.H. Wu, Y. Guo, H. Wua, Y. Zhang, H. Liu, Natural Silk cocoon derived nitrogen-doped porous carbon nanosheets for high performance lithium-sulfur batteries, Electrochim. Acta 227 (2017) 7–16, https://doi.org/10.1016/j.electacta.2016.11.139.
[35] S. Porada, P.M. Biesheuvel, V. Presser, Comment on sponge-templated preparation of high surface area graphene with ultrahigh capacitive deionization performance, Adv. Funct. Mater. 25 (2015) 175–181, https://doi.org/10.1002/adfm.201401101.
[36] Y. Liu, L.H. Wang, Q.F. Yao, X. Gao, X. Du, X.Y. Dou, H.G. Zhu, X. Yuan, J.P. Xie, In-situ synthesis of bismuth nanoclusters within carbon nano-bundles from metal-organic framework for chloride-driven electrochemical deionization, Adv. Funct. Mater. 2110087 (2022), https://doi.org/10.1002/adfm.202110087.
[37] G.J. Zhang, W.Y. Li, Z.X. Chen, J.L. Long, C. Xu, Freestanding n-doped graphene membrane electrode with interconnected porous architecture for efficient capacitive deionization, Carbon 187 (2022) 86-96, 10.1016/j.carbon.2021.10.081.
[38] S. Kundu, T.C. Nagaiah, W. Xia, Y.M. Wang, S.V. Dommele, J.H. Bitter, M. Santa, G. Grundmeier, M. Bron, W. Schuhmann, M. Muhler, Electrocatalytic activity and stability of nitrogen-containing carbon nanotubes in the oxygen reduction reaction, J. Phys. Chem. C 113 (32) (2009) 14302–14310, https://doi.org/10.1021/jp811320d.
[39] Q. Long, W. Chen, H. Xu, X. Xiong, J. Yan, Z. Feng, X. Hu, X. Ying, Z. Zhang, Y. Huang, Synthesis of functionalized 3D hierarchical porous carbon for high-performance supercapacitors, Energ. Environ. Sci. 6 (8) (2013) 2497–2504, https://doi.org/10.1039/c3ee41638k.
[40] Y. Kim, Y. Noh, J. Bae, H. Ahn, M. Kim, W.B. Kim, N-doped carbon-embedded TiN nanowires as a multifunctional separator for Li-S batteries with enhanced rate capability and cycle stability, J. Energy. Chem. 57 (2021) 10–18, https://doi.org/10.1016/j.jechem.2020.08.050.
[41] L. Wu, Y. Li, Z. Fu, B.L. Su, Hierarchically structured porous materials: synthesis strategies and applications in energy storage, Natl. Sci. Rev. 7 (11) (2020) 1667–1701, https://doi.org/10.1093/nsr/nwaa183.
[42] M. Kim, T. Park, C. Wang, J. Tang, H. Lim, M.S.A. Hossain, M. Konarova, J.W. Yi, J. Na, J. Kim, Y. Yamauchi, Tailored nanoarchitecturing of microporous ZIF-8 to hierarchically porous double-shell carbons and their intrinsic electrochemical property, ACS Appl. Mater. Interfaces 12 (30) (2020) 34065–34073, https://doi.org/10.1021/acsami.0c07467.
[43] N.L. Liu, L.L. Chen, S.Wei Tsaia, C.H Hou, Enhanced desalination of electrospun activated carbon fibers with controlled pore structures in the electrosorption process, Environ. SCI-WAT. Res. 6 (2) (2020) 312-320, 10.1039/C9EW00751B.
[44] M. Kim, X.T. Xu, R.J. Xin, J. Earnshaw, A. Ashok, J. Kim, T. Park, A.K. Nanjundan, W.A. El-Said, J.W. Yi, J. Na, Y. Yamauchi, KOH-Activated hollow ZIF–8 derived porous carbon: nanoarchitectured control for upgraded capacitive deionization and supercapacitor, ACS Appl. Mater. Interfaces 44 (2021) 52034–52043, https://doi.org/10.1021/acsami.1c09107.
[45] J. Deng, T. Xiong, F. Xu, M. Li, C. Han, Y. Gong, H. Wang, Y. Wang, Inspired by bread leavening: one-pot synthesis of hierarchically porous carbon for supercapacitors, Green Chem. 17 (2015) 4053–4060, https://doi.org/10.1016/10.1039/c5gc00523j.
[46] S. Fleischmann, J.B. Mitchell, R. Wang, C. Zhan, D.E. Jiang, V. Presser, V. Augustyn, Pseudocapacitance: from fundamental understanding to high power energy storage materials, Chem. Rev. 120 (2020) 6738–6782, https://doi.org/10.1021/acs.chemrev.0c00170.
[47] Y. Liu, X. Du, Z.P. Wang, L.Y. Zhang, Q.L. Chen, L.H. Wang, Z.Z. Liu, X.Y. Dou, H. G. Zhu, X. Yuan, $MoS_2$ nanoflakes-coated electrospun carbon nanofibers for "rocking-chair" capacitive deionization, Desalination 520 (2021), 115376, https://doi.org/10.1016/j.desal.2021.115376.
[48] G.Z. Wang, T.T. Yan, J.J. Shen, J.P. Zhang, D.S. Zhang, Capacitive removal of fluoride ions via creating multiple capture sites in a modulatory heterostructure, Environ. Sci. Technol. 55 (2021) 11979–11986, https://doi.org/10.1021/acs.est.1c03228.
[49] T. Kim, J. Yoon, CDI ragone plot as a functional tool to evaluate desalination performance in capacitive deionization, RSC Adv. 5 (2015) 1456–1461, https://doi.org/10.1039/c4ra11257a.
[50] C.L. Yeh, H.C. Hsi, K.C. Li, C.H. Hou, Improved performance in capacitive deionization of activated carbon electrodes with a tunable mesopore and micropore ratio, Desalination 367 (2015) 60–68, https://doi.org/10.1016/j.desal.2015.03.035.
[51] A.M. Dehkhoda, N. Ellis, E. Gyenge, Effect of activated biochar porous structure on the capacitive deionization of NaCl and $ZnCl_2$ solutions, Micropor. Mesopor. Mat. 224 (2016) 217–228, https://doi.org/10.1016/j.micromeso.2015.11.041.
[52] M. Liu, M. Xu, Y. Xue, W. Ni, S. Huo, L. Wu, Z. Yang, Y. Yan, Efficient capacitive deionization using natural basswood derived, free standing, hierarchically porous carbon electrodes, ACS Appl. Mater. Interfaces 10 (2018) 31260–31270, 10.1021/acsami.8b08232.
[53] Z. Xie, X. Shang, J. Yan, Hussain T, P. Nie, J. Liu, Biomass derived porous carbon anode for high-performance capacitive deionization, Electrochim. Acta 290 (2018) 666–675, 10. 1016/j.electacta.2018.09.104.

[54] G. Wang, B. Qian, Q. Dong, J. Yang, Z. Zhao, J. Qiu, Highly mesoporous activated carbon electrode for capacitive deionization, Sep. Purif. Technol. 103 (2013) 216–221, https://doi.org/10.1016/j.seppur.2012.10.041.
[55] C. Yan, L. Zou, R. Short, Polyaniline-modified activated carbon electrodes for capacitive deionisation, Desalination 333 (2014) 101–106, https://doi.org/10.1016/j.desal.2013.11.032.
[56] X. Gao, A. Omosebi, N. Holubowitch, A. Liu, K. Ruh, J. Landon, K. Liu, Polymer-coated composite anodes for efficient and stable capacitive deionization, Desalination 399 (2016) 16–20, https://doi.org/10.1016/j.desal.2016.08.006.
[57] Y. Zhang, L. Ji, Y. Zheng, H. Liu, X. Xu, Nanopatterned metal–organic framework electrodes with improved capacitive deionization properties for highly efficient water desalination, Sep. Purif. Technol. 234 (2020), 116124, https://doi.org/10.1016/j.seppur.2019.116124.
[58] A.B. Ganganboina, R.A. Doong, Nitrogen doped graphene quantum dot-decorated earth-abundant nanotubes for enhanced capacitive deionization, Environ. Sci. Nano 7 (2020) 228, https://doi.org/10.1039/c9en00852g.
[59] H. Wang, D. Zhang, T. Yan, X. Wen, J. Zhang, L. Shi, Q. Zhong, Three-dimensional macroporous graphene architectures as high performance electrodes for capacitive deionization, J. Mater. Chem. A 1 (2013) 11778–11789, https://doi.org/10.1039/c3ta11926b.
[60] X.D. Ma, X.H. Xiong, J.Q. Zeng, P.J. Zou, Z. Lin, M.L. Liu, Melamine-assisted synthesis of $Fe_3N$ featuring highly reversible crystalline-phase transformation for ultrastable sodium ion storage, J. Mater. Chem. A 8 (2020) 6768–6775, https://doi.org/10.1039/d0ta01888k.
[61] H. Zhang, Q.Y. Wang, J. Zhang, G. Chen, Z.W. Wang, Z.C. Wu, Development of novel ZnZr-COOH/CNT composite electrode for selectively removing phosphate by capacitive deionization, Chem. Eng. J. 439 (2022), 135527, https://doi.org/10.1016/j.cej.2022.135527.
[62] X.T. Xu, A.E. Allah, C. Wang, H.B. Tan, A.A. Farghali, M.H. Khedrd, V. Malgras, T. Yang, Y. Yamauchi, Capacitive deionization using nitrogen-doped mesostructured carbons for highly efficient brackish water desalination, Chem. Eng. J. 362 (2019) 887–896, https://doi.org/10.1016/j.cej.2019.01.098.